THE JOURNAL OF PHYSICAL CHEMISTRY LETTERS
A JOURNAL OF THE AMERICAN CHEMICAL SOCIETY

pubs.acs.org/JPCL

Letter

A Quantum Monte Carlo Study of the Structural, Energetic, and Magnetic Properties of Two-Dimensional H and T Phase VSe_2

Daniel Wines, Juha Tiihonen, Kayahan Saritas, Jaron T. Krogel, and Can Ataca*

Cite This: *J. Phys. Chem. Lett.* 2023, 14, 3553−3560

Read Online

ACCESS | Metrics & More | Article Recommendations | Supporting Information

ABSTRACT: Previous works have controversially claimed near-room-temperature ferromagnetism in two-dimensional (2D) VSe_2, with conflicting results throughout the literature. These discrepancies in magnetic properties between both phases (T and H) of 2D VSe_2 are most likely due to the structural parameters being coupled to the magnetic properties. Specifically, both phases have a close lattice match and similar total energies, which makes it difficult to determine which phase is being observed experimentally. In this study, we used a combination of density functional theory, highly accurate diffusion Monte Carlo (DMC), and a surrogate Hessian line-search optimization technique to resolve the previously reported discrepancy in structural parameters and relative phase stability. With DMC accuracy, we determined the free-standing geometry of both phases and constructed a phase diagram. Our findings demonstrate the successes of the DMC method coupled with the surrogate Hessian structural optimization technique when applied to a 2D magnetic system.

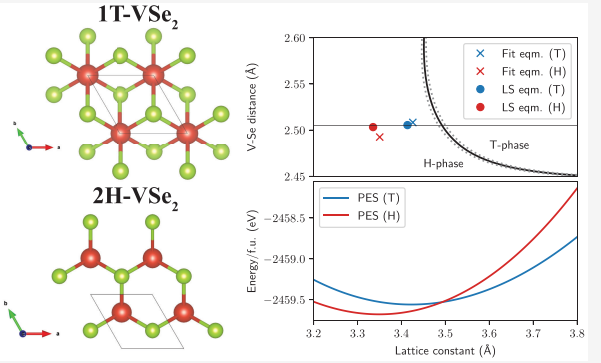

One of the most promising two-dimensional (2D) magnetic materials that has been extensively studied experimentally and theoretically is 2D VSe_2. Similar to other 2D transition metal dichalcogenides (such as MoS_2),[1] VSe_2 exists in two phases, the T [octahedral phase (1T)-centered honeycombs] phase that is metallic and the H [the trigonal prismatic phase (2H)-hexagonal honeycombs (see Figure 1)] phase that is semiconducting. Several experimental and theoretical studies have controversially claimed near-room-temperature ferromagnetism in VSe_2, with conflicting results throughout the literature. Density functional theory (DFT) along with classical Monte Carlo simulations have been used to obtain an estimate of the Curie temperature of H-VSe_2 (291 K),[2] but the model Ising Hamiltonian used did not take into account the magnetic anisotropy energies, which are essential for an accurate estimation of the Curie temperature of a 2D lattice. The Curie temperature of multilayered 2D H-VSe_2 has been experimentally measured to be 425 K, with the ferromagnetism softening as the thickness of the sample increases.[3] Additionally, the experimental Curie temperature for monolayer T-VSe_2 has ranged from 300 to 470 K[4,5] depending on which substrate is used (MoS_2, graphite, or SiO_2-coated silicon). The experimental magnetization of T-VSe_2 has also been met with controversy, with values of 15 and 5 μ_B [per formula unit (f.u.)] being reported from two separate studies.[4,6] Insight has also been reported with regard to how the ferromagnetism is enhanced with defects, molecular adsorption, and the choice of substrate for VSe_2.[4,5,7] Although recent reports have suggested that T-VSe_2 could be experimentally paramagnetic,[3] it is possible that this paramagnetism can be induced by magnetic anisotropy. In addition, a wide range of values have also been reported for the charge density wave (CDW) transition temperature for T-VSe_2, ranging from 120 to 350 K.[3,6,8−10]

These discrepancies in the electronic and magnetic properties of either phase of 2D VSe_2 arise from the structural parameters of each phase being coupled closely to the magnetic and electronic properties and the external factors (substrates and defects) of the individual samples. One example of this has been a reported discrepancy in which phase (T or H) is energetically more favorable. The T and H phases have a close lattice match and similar total energies, which makes it difficult to determine which phase is being observed experimentally. Recently, it has been reported experimentally that the T phase is favored for bulk VSe_2, but with a decrease in dimensionality, the H phase is favored.[3,11] It has also been reported that a T-to-H phase transition can be realized by thermal annealing.[11] This same structural phase transition has even been reported by applying a biaxial strain of ≈3% (from the calculated results).[7,11,12] Researchers have

Received: February 21, 2023
Accepted: March 30, 2023
Published: April 5, 2023

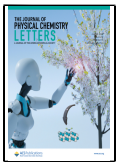

https://doi.org/10.1021/acs.jpclett.3c00497
J. Phys. Chem. Lett. 2023, 14, 3553−3560

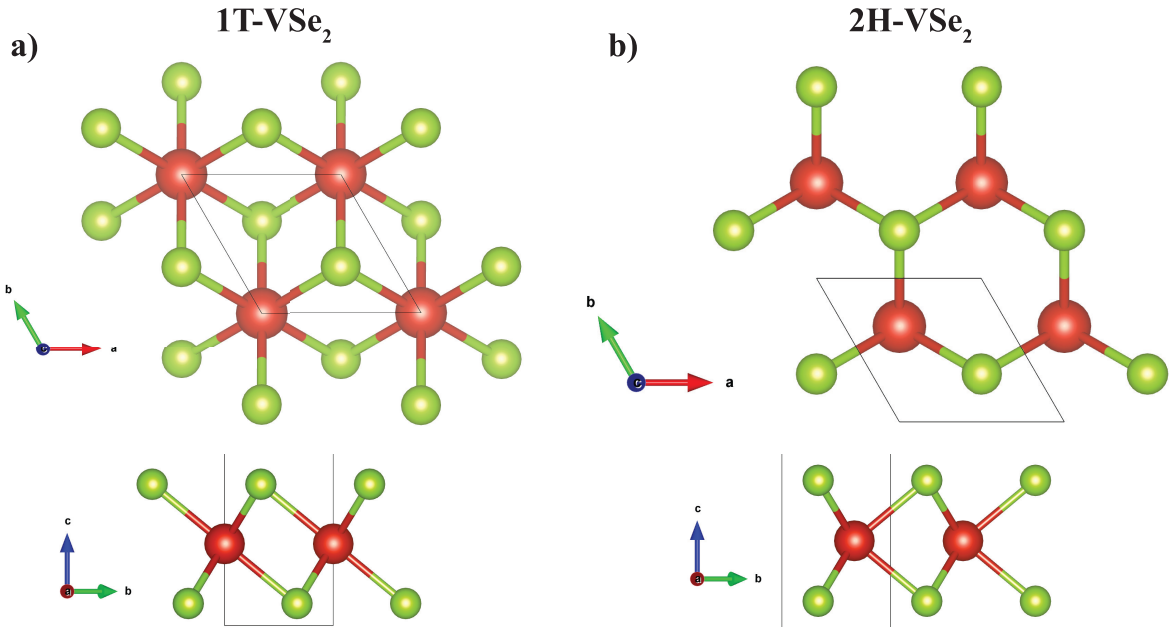

Figure 1. Top and side views of the atomic structure of monolayer VSe_2 in the (a) 1T and (b) 2H phases.

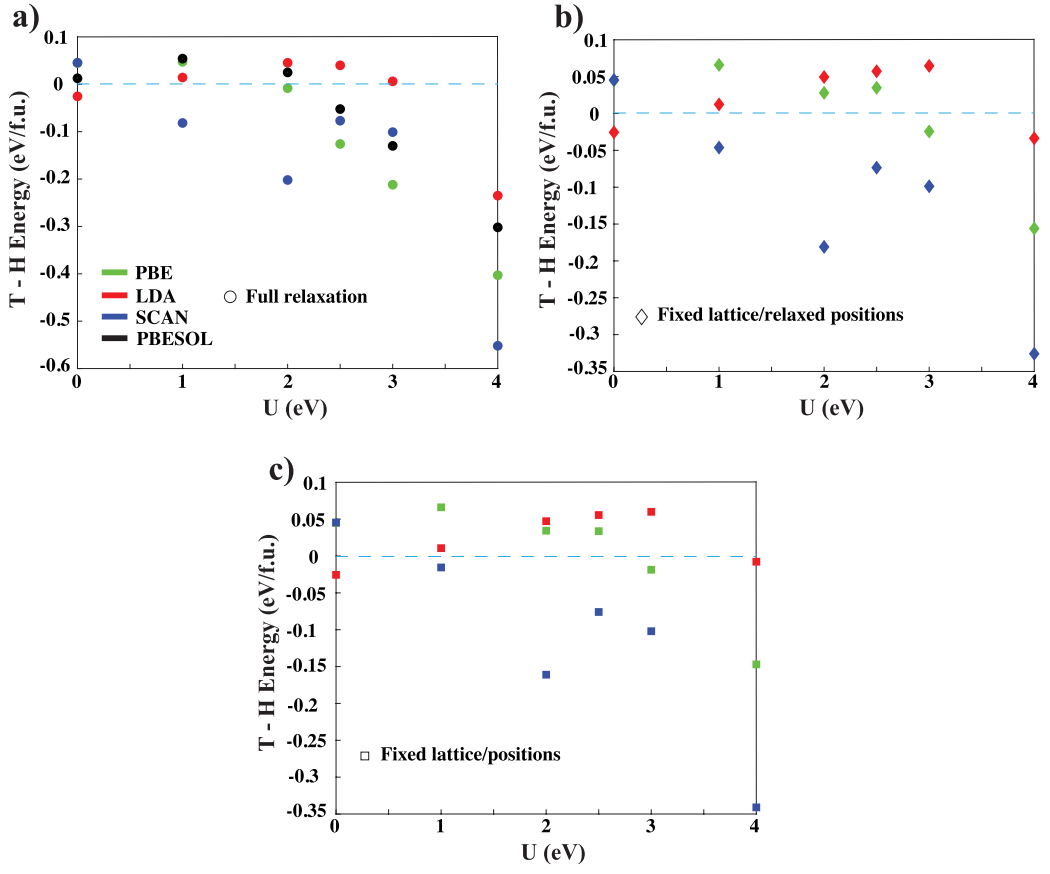

Figure 2. Relative (T − H) energy between T and H phase 2D VSe_2 as a function of the U parameter for several density functionals and methods of atomic relaxation: (a) fully relaxing the structure, (b) fixing the lattice and atomic positions to the U = 0 eV relaxed geometry of that particular functional and calculating the static energy, and (c) fixing the lattice to the U = 0 eV relaxed geometry of that particular functional and relaxing just the atomic positions. The dotted line indicates 0 eV.

proposed that this lattice strain can be induced by the mismatch that occurs from placing 2D VSe_2 on a substrate.[7,12]

From a computational perspective, the results for VSe_2 depend strongly on which methodology is employed. In most cases, DFT with an empirical Hubbard correction ($+U$) for correlated electrons is used.[13] For example, if the U correction is applied for T- and H-VSe_2, the T phase is more energetically favorable, while if no U correction is applied, the

https://doi.org/10.1021/acs.jpclett.3c00497
J. Phys. Chem. Lett. 2023, 14, 3553−3560

Table 1. Lattice Constants, V−Se Distances, and Relative Energies (T − H) for T and H Phase 2D VSe_2 for Several Computational Methods[a]

	T-VSe_2		H-VSe_2		
method	a (Å)	d^{V-Se} (Å)	a (Å)	d^{V-Se} (Å)	E^{T-H} (eV/f.u.)
PBE	3.336	2.489	3.333	2.502	0.045
PBE+U=2	3.435	2.526	3.364	2.520	−0.008
LDA	3.228	2.438	3.229	2.445	−0.026
LDA+U=2	3.277	2.455	3.266	2.464	0.045
SCAN	3.387	2.486	3.329	2.486	0.045
SCAN+U=2	3.462	2.524	3.353	2.502	−0.202
PBEsol	3.262	2.458	3.272	2.471	0.013
PBEsol+U=2	3.323	2.483	3.301	2.487	0.025
PBE-D2	3.323	2.484	3.318	2.496	0.010
PBE-D3	3.315	2.485	3.319	2.497	0.042
SCAN+rvv10	3.379	2.481	3.319	2.482	0.051
DMC	3.414(12)	2.505(7)	3.335(8)	2.503(5)	0.06(2)

[a]The energy difference is given per formula unit (f.u.). DMC error bars (standard error of the mean) are included in parentheses.

H phase is more favorable.[14] In addition to the discrepancies in results calculated with DFT+U, results between van der Waals (vdW)-corrected functionals and hybrid functionals are also inconclusive[14] in terms of predicting the relative phase stability. To alleviate the uncertainty in DFT methods, more sophisticated methods can be used such as diffusion Monte Carlo (DMC).[15] DMC is a correlated, many-body electronic structure method that has been demonstrated to have success for the electronic and magnetic properties of a variety of bulk and 2D systems.[16−24] This method has a weaker dependence on the starting density functional and U parameter and can successfully achieve results with an accuracy beyond the DFT +U.[15]

Due to the fact that T- and H-VSe_2 have structural parameters that are coupled to their electronic and magnetic properties, it makes it difficult to produce conclusive results that rely solely on DFT or DFT+U. For this reason, we employed our recently developed energy-based surrogate Hessian method for structural optimization with stochastic electronic structure theories (such as DMC)[22] to obtain the geometric structure of T- and H-VSe_2 with DMC accuracy, resulting in high-accuracy bond lengths that resolve previous functional-dependent structural discrepancies. After obtaining an accurate geometry for both structures, we constructed a phase diagram between T- and H-VSe_2 using DMC-calculated energies and obtained accurate magnetic properties of each structure. The accurate estimates of the lattice geometry, relative phase energy, and DMC phase diagram assist in clarifying previously inconclusive theoretical and experimental results with regard to T and H phase VSe_2. It is important to note that the modeling of paramagnetism with computational methods imposes a great challenge, requiring the simulation of large supercells with different magnetizations, which is why we focus on the free-standing ferromagnetic ground states of both phases. A more robust treatment of the magnetic structure can be explored in the future but is beyond the scope of this work, which primarily focuses on determining the geometric structure and phase stability of 2D T- and H-VSe_2. For full details of the computational methods used, see the Supporting Information.

As an initial starting point for our study, we performed benchmarking DFT and DFT+U calculations using a variety of density functionals [local density approximation (LDA),[25] Perdew−Burke−Ernzerhof (PBE),[26] and strongly constrained and appropriately normed (SCAN)[27] meta-GGA functionals (see the Supporting Information for more details)] and the Vienna Ab initio Simulation Package (VASP) code for monolayer T-VSe_2 and H-VSe_2. The goal of these simulations was to assess how sensitive the relative energy between the T and H phase is with respect to functional and material geometry. Another goal of these simulations was to benchmark the structural parameters of each material with respect to several density functionals. It is advantageous to perform these reference calculations with VASP and projector-augmented wave (PAW) pseudopotentials[28,29] as a precursor to the more expensive DMC calculations due to the fact that they require a much smaller cutoff energy and are more cost-effective for a large number of simulations. It is important to note that for all DFT and DMC simulations, we assumed a ferromagnetic ground state for both T- and H-VSe_2.

In Figure 2, we present a comprehensive look at the difference in total energy between T-VSe_2 and H-VSe_2, using several DFT functionals under different geometric constraints. We performed these calculations for a variety of U values in three different ways: fully relaxing the structure at each value of U (Figure 2a), fixing the lattice and atomic positions to the U = 0 eV relaxed geometry of that particular functional and calculating the static energy at each value of U (Figure 2b), and fixing the lattice to the U = 0 eV relaxed geometry of that particular functional and relaxing just the atomic positions at each value of U (Figure 2c). The results in Figure 2 indicate that there is a significant disagreement between DFT functionals, U value used, and material geometries, with all three factors playing a significant role in the energy difference between the T and H phases. Specifically, regardless of the relaxation method, all bare (no U correction) SCAN, PBE, and PBEsol functionals predict H favorable while bare LDA predicts T favorable. For all functionals, there is a critical value of U that reverses the relative phase stability, which is dependent on the functional and relaxation method. The SCAN functional with a U correction predicts T phase favorable, with larger energy differences. As shown in Figure 2, the trends in the relative phase stability between panels b and c of Figure 2 are nearly identical but significantly vary from those in panel a of Figure 2. This implies that the density functional is strongly coupled to material geometry, but the lattice constant change has a stronger effect on phase stability than atomic positions and bond distances. This is most prevalent for

https://doi.org/10.1021/acs.jpclett.3c00497
J. Phys. Chem. Lett. 2023, 14, 3553−3560

higher U values (>2 eV), where the relaxed geometry changes more drastically with U. The interrelated nature of the material's geometry, density functional, and value of U are reasons to seek out higher levels of theory beyond DFT/DFT +U such as DMC to accurately determine the optimal geometry and relative energy between the phases of 2D VSe_2.

The relaxed lattice constants, V−Se distances, and T − H energies from Figure 2a are listed in Table 1 and Figure 3,

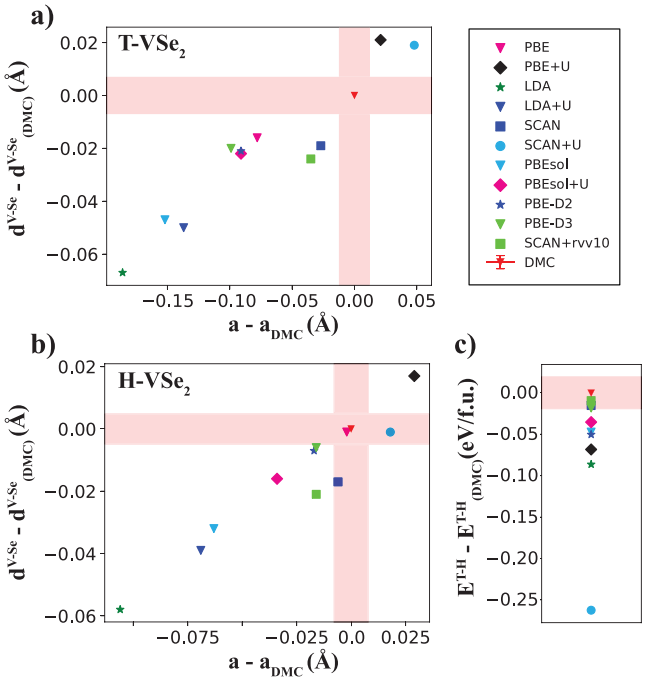

Figure 3. Summary of the deviation of the geometric properties relative to the DMC-calculated geometric properties for (a) T-VSe_2 and (b) H-VSe_2 and (c) deviation of the T − H energy relative to the DMC-calculated T − H energy for a variety of DFT functionals (U = 2 eV), where the DMC error bar (standard error of the mean) is represented by the red bars.

along with additional VASP reference calculations performed with the vdW-corrected functionals (PBE-D2,[30] PBE-D3,[31] and SCAN+rvv10[32]). The DMC-computed parameters are also given for comparison in Table 1 and Figure 3 (more discussion to follow). We observe an ≈7% variability in the lattice constant across the different methods for T-VSe_2 and an ≈4% variability in the lattice constant across the different methods for H-VSe_2. Between both phases, we observe an ≈3% variability in the V−Se distance (d^{V-Se}). To contextualize our results with recent theoretical calculations of 2D T-VSe_2 (which used a widely adapted effective U value of 3 eV[14,33,34]), we note that our lattice constant results for PBEsol+U=2 are in excellent agreement with recently reported PBEsol U = 3 results (within 1%).[33] Most strikingly, the energy difference between the T and H phases (E^{T-H}) drastically varies depending on the material geometry and computational methodology, ranging from −0.2 to 0.06 eV/f.u. Due to the fact that a strain-induced phase transition has been reported between T- and H-VSe_2,[7,11,12] we decided to perform additional VASP benchmarking calculations that involved the application of tensile and compressive strain for each monolayer. We performed these calculations for PBE, SCAN, and LDA (with U = 0 eV and U = 2 eV), starting from the U = 0 eV geometry for each functional. The resulting equations of state are depicted in Figure S3. As shown in the figure, the equation of state and resulting strain-induced phase transition are entirely dependent on the functional and U value, with no consistent trend.

The strong sensitivity of each monolayer with respect to geometry and functional is grounds for using a higher-order method such as DMC to obtain a statistically accurate estimate of the lattice parameters and relative energy between phases. Prior to performing the DMC/line-search calculations, we optimized our nodal surface (orbitals selected for DFT wave function generation). Because DMC has a zero-variance property, this means that as the trial wave function approaches the exact ground state, the statistical fluctuations in the energy decrease to zero.[15] Although there have been instances in which various sophisticated methods have been used to optimize the nodal surface,[35−38] we employed the PBE+U approach, where the Hubbard (U) value was used as a variational parameter to optimize the nodal surface using DMC (similar to other successful DMC studies of magnetic materials[16,20,21,24,39−41]). We performed these calculations for both T- and H-VSe_2 (24-atom supercells), where we tuned the U value from 1 to 4 eV while creating the trial wave function and computed the DMC energy. The results of these calculations are depicted in Figure 4, where we observe that

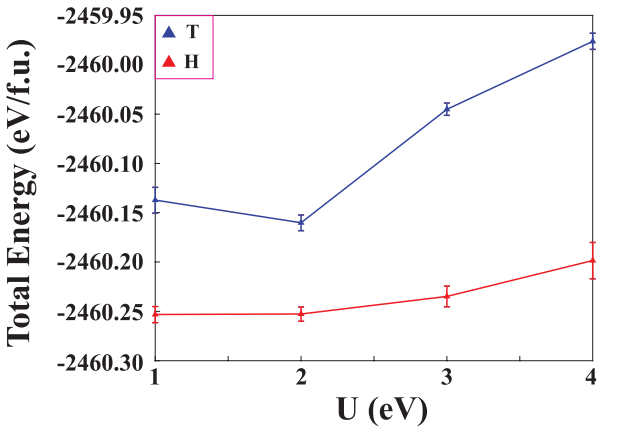

Figure 4. DMC-calculated total energies of a 24-atom supercell [normalized per formula unit (f.u.)] of 2D T (blue) and H (red) phase VSe_2 calculated as a function of the U parameter used to variationally determine the optimal trial wave function. The DMC error bars represent the standard error of the mean.

a U of 2 eV yields the lowest energy for both phases. It is important to note that for the H phase, the DMC energies for U values of 1 and 2 eV are statistically identical. On this basis, we created the trial wave function using PBE+U (U = 2 eV) for all subsequent DMC calculations within the surrogate Hessian line search for both phases (all 52 DMC energy evaluations). Because we obtained an optimal U value of 2 eV for both materials, we focused our DFT+U benchmarking efforts more on a U value of 2 eV (Figures 2, 3, and 6, Table 1, and Figure S3).

On the basis of the DMC line-search results, we determined accurate bounds on the lattice parameter (a) and off-plane displacement of Se (z), within an error tolerance of ≤0.018 Å for both parameters. This translates to within ≈0.5% accuracy in a parameter set of a and d^{V-Se} with 95% statistical confidence. Convergence (absence of significant displacements

https://doi.org/10.1021/acs.jpclett.3c00497
J. Phys. Chem. Lett. 2023, 14, 3553−3560

outside of the error tolerance) was achieved after two parallel line-search iterations for both phases. This convergence is illustrated in Figure S4, where the convergence of the parameter offsets of a and z and the convergence of the total energy per formula unit are depicted for both T and H phase 2D VSe_2 for the initial DFT-relaxed structure (1) and both subsequent iterations of DMC (2 and 3). In addition, the final energies of both of the fitted structures (squares) are given.

The final geometric parameters and relative phase energies determined with DMC are listed in Table 1 and Figure 3. For T-VSe_2, we determined a lattice constant of 3.414(12) Å and a V−Se distance of 2.505(7) Å. For H-VSe_2, we determined a lattice constant of 3.335(8) Å and a V−Se distance of 2.503(5) Å. The DMC finite-size extrapolated energy difference (T − H) between the two phases was determined to be 0.06(2) eV/f.u., indicating that in free-standing form at the equilibrium geometry, H-VSe_2 is favored over T-VSe_2. Upon comparison of these DMC results to the other DFT functionals in Table 1 and Figure 3, it is clear that very few DFT functionals can reproduce the DMC results for the lattice constant, V−Se distance, and relative energy difference. The SCAN functional comes the closest to reproducing all three simultaneous DMC values but still falls slightly short for the V−Se distances of both phases and the lattice constant of T-VSe_2. The fact that SCAN+U successfully predicts the structural properties (for H-VSe_2) and the fact that SCAN+rvv10 produces an energy difference closest to the average DMC energy difference for both phases loosely imply that a simultaneous description of correlated magnetism and vdW interactions is needed to correctly represent the physics of VSe_2. Experimental measurements of the lattice constant and V−Se distance of free-standing monolayer VSe_2 are scarce and often dependent on external factors such as the substrate (more discussion to follow) and sample preparation technique.[4,5,42,43] However, Chen et al.[42] have recently reported a lattice constant of 3.4 Å for thin films of T-VSe_2, and Liu et al.[43] have recently reported a lattice constant of 3.3 Å for epitaxially grown monolayer H-VSe_2. Both of these measured values are in excellent agreement with our DMC-computed lattice constants. Additionally, we determined the near-equilibrium PES of both T and H 2D VSe_2 with DMC accuracy, which are both depicted in Figure S5.

The phase diagram presented in Figure 5 is based on similar fits to data, where the z displacement has been remapped to d^{V-Se}. This DMC phase diagram can directly be compared to the energy versus strain DFT benchmarking calculations in Figure S3, which emphasizes the need for an accurate representation of the phase boundary between the two phases. The free-standing geometries of both T and H lie in the energetic H phase, but a slice of the phase diagram along a d^{V-Se} of 2.505 Å indicates that the T phase becomes favorable over H at biaxial strain of approximately $a \geq 3.5$ Å. This implies that in free-standing form, once T-VSe_2 is positively strained at least ≈2.5%, the T phase is favored over H. Alternatively, if free-standing H-VSe_2 is positively strained at least ≈5%, the T phase is also favored over H. This strain can easily be accomplished by placing monolayer VSe_2 on a substrate with a significant lattice mismatch. In fact, this type of mismatch has been reported to alter the material properties,[4,5,44,45] significantly contributing to the controversies of T- and H-VSe_2 (for energetic favorability and magnetic properties). Whether the changes in energetic favorability or magnetic properties with respect to the substrate are due to

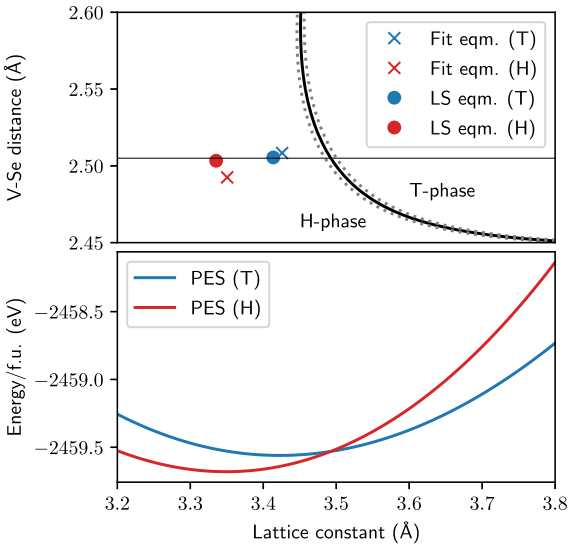

Figure 5. Phase diagram of 2D VSe_2 in terms of a and d^{V-Se} (top). The phase boundary (solid black line) is estimated from bicubic fits. To ensure the quality of the fits, the estimated ±0.01 eV error contours (dotted line) and the minima from the bicubic fits (times signs, Fit eqm.) and the line search (circles, LS eqm.) are all well separated. Slices of the PES at d^{V-Se} = 2.505 Å (bottom).

lattice mismatch or more complicated interactions between the substrate and the monolayer remains to be answered and is beyond the scope of this work, which has focused solely on the free-standing forms of T- and H-VSe_2. However, such calculations can be employed for future work using higher-order methods such as DMC. The proximity of the phase boundary between the T and H phases (Figure 5) is emphasized by the small energy difference between the two phases [0.06(2) eV/f.u., at the equilibrium geometry] between the two curves. Because this energy difference is so close to room temperature (≈0.024 eV), this implies that a process such as thermal annealing can easily induce a phase transition. In fact, recently it was demonstrated that a structural phase transition of multilayer VSe_2 from T to H occurs through annealing at 650 K, along with a metal−insulator transition.[11]

To gain a deeper understanding of the magnetic properties of 2D T- and H-VSe_2, we extracted the spin densities (using a trial wave function at U = 2 eV and a 24-atom supercell at the final equilibrium geometry predicted by DMC/line search). We went on to plot the radially averaged spin densities as a function of distance, separately for V and Se for T- and H-VSe_2 (depicted in Figure 6a−d). This allows us to view the spatial variations in spin density. Additionally, we benchmarked these V and Se radially averaged densities with PBE+U (U = 2 eV) using NC pseudopotentials at the equilibrium geometry (the calculation required to create the trial WF for the subsequent DMC runs). As shown in panels a and c of Figure 6, there is a substantial difference in the V spin density between DMC and PBE+U (U = 2 eV) for both T and H phases. This same substantial difference between DMC and PBE+U also occurs for the total charge density. This discrepancy is most prevalent near the radial density peak (peak of the d orbital) and can be attributed to the fact that DFT functionals (even with the added Hubbard correction) tend to delocalize and unsuccessfully capture 3d orbitals. This large discrepancy in the spin densities highlights the need for more accurate, many-body computational methodologies for correlated materials such as

https://doi.org/10.1021/acs.jpclett.3c00497
J. Phys. Chem. Lett. 2023, 14, 3553−3560

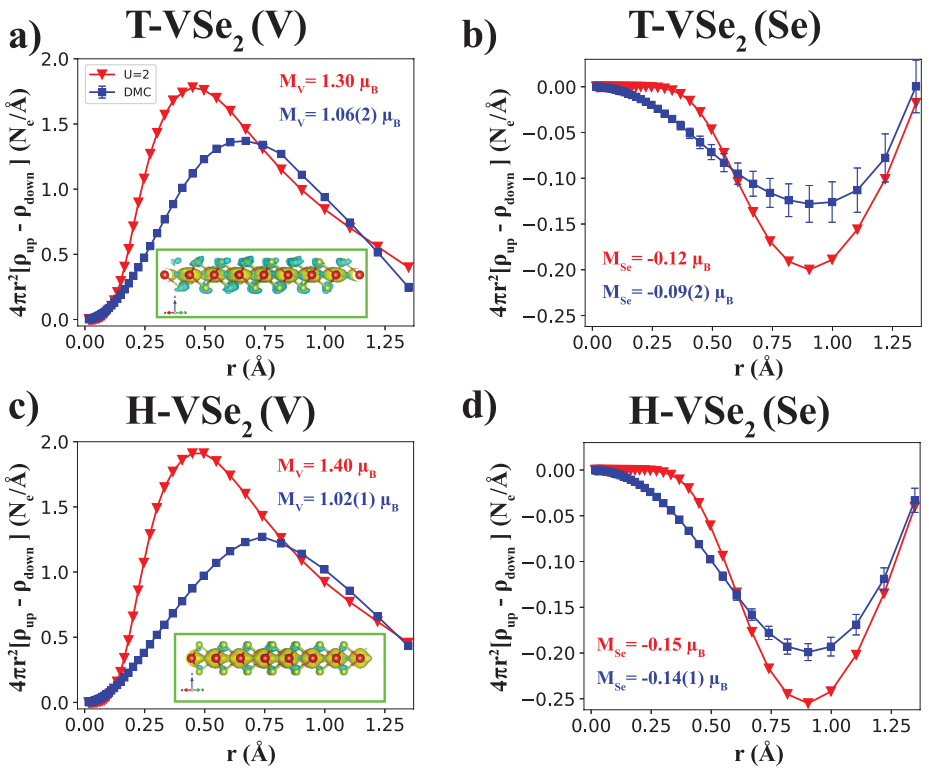

Figure 6. Radially averaged spin density ($\rho_{up} - \rho_{down}$) as a function of distance, calculated with DMC and PBE+U (U = 2 eV) of (a) V and (b) Se for 2D T-VSe_2 and (c) V and (d) Se for 2D H-VSe_2. The insets of panels a and c depict the spin isosurface density of T-VSe_2 and H-VSe_2, respectively, where the isosurface value was set to 6×10^{-3} e/Å^3. The standard error of the mean for DMC is indicated by blue error bars.

VSe_2, where DFT fails. In contrast, there is closer agreement between the DMC and PBE+U spin densities for Se in T- and H-VSe_2 (see Figure 6b,d). The spin density isosurfaces of each phase ($\rho_{up} - \rho_{down}$) are depicted in the insets of panels a and c of Figure 6 for T-VSe_2 and H-VSe_2, respectively. For both phases, we observe the V atoms are highly spin-polarized, while the Se atoms are slightly antiparallel with respect to the V atoms. For more calculation details with regard to spin density, see the Supporting Information.

Finally, we estimated the site-averaged atomic magnetic moments per V and Se for both T and H phases by integrating the DMC and PBE+U spin densities depicted in Figure 6. At the DMC level, we estimated magnetic moments of 1.06(2) μ_B for V and −0.09(2) μ_B for Se in T-VSe_2 and magnetic moments of 1.02(1) μ_B for V and −0.14(1) μ_B for Se in H-VSe_2. At the PBE+U (U = 2 eV) level, we estimated magnetic moments of 1.30 μ_B for V and −0.12 μ_B for Se in T-VSe_2 and magnetic moments of 1.40 μ_B for V and −0.15 μ_B for Se in H-VSe_2. Consistent with the radial spin density results in Figure 6, we find that the DMC and PBE+U magnetic moments for Se are in much closer agreement than for V (for both T and H phases). By analyzing the spin densities and obtaining the on-site magnetic moments, we obtain a clear picture of how the magnetization of each ion depends on the computational method used, serving as a benchmark for the magnetic properties of 2D VSe_2.

In this work, we used a combination of DFT, DMC, and a recently developed surrogate Hessian line-search optimization technique to resolve the previously reported discrepancy in structural parameters and relative phase stability of monolayer T-VSe_2 and H-VSe_2. Using these methods, we determined the lattice constant and V−Se distance (with DMC accuracy) to be 3.414(12) and 2.505(7) Å, respectively, for T-VSe_2 and 3.335(8) and 2.503(5) Å, respectively, for H-VSe_2. In addition, we find the relative energy between the phases (T − H) to be 0.06(2) eV/f.u. at the DMC level, indicating that in free-standing form, H-VSe_2 is more energetically favorable than T-VSe_2. We went on to obtain a phase diagram between T and H phases from the potential energy surface (PES) and determined that a phase transition can be induced by strain or mechanisms such as thermal annealing. Additionally, we benchmarked the magnetic properties such as spin density and on-site magnetic moment for both phases and find substantial differences between DMC and DFT. The results of this study demonstrate the successes of the DMC method coupled with the surrogate Hessian line-search structural optimization technique when applied to a 2D magnetic system. The estimates for the lattice constant, bond distance, relative phase energy, and extracted structurally dependent phase diagram assist in clarifying previously inconclusive theoretical and experimental results with regard to T and H phase VSe_2.

■ ASSOCIATED CONTENT

Data Availability Statement

The data from this work are available at https://figshare.com/projects/2D_VSe2_Quantum_Monte_Carlo/162613.

Supporting Information

The Supporting Information is available free of charge at https://pubs.acs.org/doi/10.1021/acs.jpclett.3c00497.

Computational details of DFT and QMC, plane wave cutoff converge, k-point convergence, time step convergence, details of spin density estimator, additional details of the surrogate Hessian accelerated optimization method, additional DFT benchmarking, and further

https://doi.org/10.1021/acs.jpclett.3c00497
J. Phys. Chem. Lett. 2023, 14, 3553−3560

details of the line-search convergence and potential energy surfaces (PDF)
Transparent Peer Review report available (PDF)

Accession Codes

Software packages mentioned in the article can be found at https://github.com/usnistgov/jarvis. Note that the use of commercial software (VASP) does not imply recommendation by the National Institute of Standards and Technology.

AUTHOR INFORMATION

Corresponding Author

Can Ataca − *Department of Physics, University of Maryland Baltimore County, Baltimore, Maryland 21250, United States;* orcid.org/0000-0003-4959-1334; Email: ataca@umbc.edu

Authors

Daniel Wines − *Materials Science and Engineering Division, National Institute of Standards and Technology (NIST), Gaithersburg, Maryland 20899, United States;* orcid.org/0000-0003-3855-3754

Juha Tiihonen − *Department of Physics, Nanoscience Center, University of Jyväskylä, 40014 Jyväskylä, Finland;* orcid.org/0000-0003-2107-911X

Kayahan Saritas − *Material Science and Technology Division, Oak Ridge National Laboratory, Oak Ridge, Tennessee 37831, United States;* orcid.org/0000-0002-2240-8520

Jaron T. Krogel − *Material Science and Technology Division, Oak Ridge National Laboratory, Oak Ridge, Tennessee 37831, United States;* orcid.org/0000-0002-1859-181X

Complete contact information is available at: https://pubs.acs.org/10.1021/acs.jpclett.3c00497

Notes

The authors declare no competing financial interest.

ACKNOWLEDGMENTS

This work was supported by the National Science Foundation through the Division of Materials Research under NSF Grant No. DMR-2213398. The authors thank the National Institute of Standards and Technology for funding, computational, and data-management resources. Work by J.T and J.T.K. (stochastic structure optimization, writing) was supported by the U.S. Department of Energy, Office of Science, Basic Energy Sciences, Materials Sciences and Engineering Division, as part of the Computational Materials Sciences Program and Center for Predictive Simulation of Functional Materials. Work by K.S. conceptual idea and writing) was supported by the U.S. Department of Energy, Office of Science, Basic Energy Sciences, Materials Sciences and Engineering Division. We acknowledge grants of computer capacity from the Finnish Grid and Cloud Infrastructure (persistent identifier urn:nbn:fi:research-infras-2016072533). The authors thank Dr. Kamal Choudhary and Dr. Francesca Tavazza for fruitful discussions.

REFERENCES

(1) Ataca, C.; Şahin, H.; Ciraci, S. Stable, Single-Layer MX_2 Transition-Metal Oxides and Dichalcogenides in a Honeycomb-Like Structure. *J. Phys. Chem. C* **2012**, *116*, 8983−8999.

(2) Fuh, H.-R.; Chang, C.-R.; Wang, Y.-K.; Evans, R. F. L.; Chantrell, R. W.; Jeng, H.-T. Newtype Single-layer Magnetic Semiconductor in Transition-metal Dichalcogenides VX_2 (X = S, Se and Te). *Sci. Rep.* **2016**, *6*, 32625.

(3) Wang, X.; Li, D.; Li, Z.; Wu, C.; Che, C.-M.; Chen, G.; Cui, X. Ferromagnetism in 2D Vanadium Diselenide. *ACS Nano* **2021**, *15*, 16236−16241.

(4) Bonilla, M.; Kolekar, S.; Ma, Y.; Diaz, H. C.; Kalappattil, V.; Das, R.; Eggers, T.; Gutierrez, H. R.; Phan, M.-H.; Batzill, M. Strong Room-temperature Ferromagnetism in VSe_2 Monolayers on van der Waals Substrates. *Nat. Nanotechnol.* **2018**, *13*, 289−293.

(5) Yu, W.; et al. Chemically Exfoliated VSe_2 Monolayers with Room-Temperature Ferromagnetism. *Adv. Mater.* **2019**, *31*, 1903779.

(6) Duvjir, G.; et al. Emergence of a Metal-Insulator Transition and High-Temperature Charge-Density Waves in VSe_2 at the Monolayer Limit. *Nano Lett.* **2018**, *18*, 5432−5438.

(7) Boukhvalov, D. W.; Politano, A. Unveiling the Origin of Room-temperature Ferromagnetism in Monolayer VSe_2: The Role of Extrinsic Effects. *Nanoscale* **2020**, *12*, 20875−20882.

(8) Sahoo, S.; Dutta, U.; Harnagea, L.; Sood, A. K.; Karmakar, S. Pressure-induced Suppression of Charge Density Wave and Emergence of Superconductivity in 1*T*−VSe_2. *Phys. Rev. B* **2020**, *101*, 014514.

(9) Feng, J.; et al. Electronic Structure and Enhanced Charge-Density Wave Order of Monolayer VSe_2. *Nano Lett.* **2018**, *18*, 4493−4499.

(10) Chen, P.; Pai, W. W.; Chan, Y.-H.; Madhavan, V.; Chou, M. Y.; Mo, S.-K.; Fedorov, A.-V.; Chiang, T.-C. Unique Gap Structure and Symmetry of the Charge Density Wave in Single-Layer VSe_2. *Phys. Rev. Lett.* **2018**, *121*, 196402.

(11) Li, D.; Wang, X.; Kan, C.-m.; He, D.; Li, Z.; Hao, Q.; Zhao, H.; Wu, C.; Jin, C.; Cui, X. Structural Phase Transition of Multilayer VSe_2. *ACS Appl. Mater. Interfaces* **2020**, *12*, 25143−25149.

(12) Pushkarev, G. V.; Mazurenko, V. G.; Mazurenko, V. V.; Boukhvalov, D. W. Structural Phase Transitions in VSe_2: Energetics, Electronic Structure and Magnetism. *Phys. Chem. Chem. Phys.* **2019**, *21*, 22647−22653.

(13) Dudarev, S. L.; Botton, G. A.; Savrasov, S. Y.; Humphreys, C. J.; Sutton, A. P. Electron-energy-loss Spectra and the Structural Stability of Nickel Oxide: An LSDA+U Study. *Phys. Rev. B* **1998**, *57*, 1505−1509.

(14) Popov, Z. I.; Mikhaleva, N. S.; Visotin, M. A.; Kuzubov, A. A.; Entani, S.; Naramoto, H.; Sakai, S.; Sorokin, P. B.; Avramov, P. V. The Electronic Structure and Spin States of 2D Graphene/VX_2 (X = S, Se) Heterostructures. *Phys. Chem. Chem. Phys.* **2016**, *18*, 33047−33052.

(15) Foulkes, W. M. C.; Mitas, L.; Needs, R. J.; Rajagopal, G. Quantum Monte Carlo Simulations of Solids. *Rev. Mod. Phys.* **2001**, *73*, 33−83.

(16) Foyevtsova, K.; Krogel, J. T.; Kim, J.; Kent, P. R. C.; Dagotto, E.; Reboredo, F. A. Ab initio Quantum Monte Carlo Calculations of Spin Superexchange in Cuprates: The Benchmarking Case of Ca_2CuO_3. *Phys. Rev. X* **2014**, *4*, 031003.

(17) Busemeyer, B.; Dagrada, M.; Sorella, S.; Casula, M.; Wagner, L. K. Competing Collinear Magnetic Structures in Superconducting FeSe by First-principles Quantum Monte Carlo Calculations. *Phys. Rev. B* **2016**, *94*, 035108.

(18) Wines, D.; Saritas, K.; Ataca, C. A First-principles Quantum Monte Carlo Study of Two-dimensional (2D) GaSe. *J. Chem. Phys.* **2020**, *153*, 154704.

(19) Wines, D.; Saritas, K.; Ataca, C. A Pathway Toward High-throughput Quantum Monte Carlo Simulations for Alloys: A Case Study of Two-dimensional (2D) GaS_xSe_{1-x}. *J. Chem. Phys.* **2021**, *155*, 194112.

(20) Wines, D.; Saritas, K.; Ataca, C. Intrinsic Ferromagnetism of Two-Dimensional (2D) MnO_2 Revisited: A Many-Body Quantum Monte Carlo and DFT+U Study. *J. Phys. Chem. C* **2022**, *126*, 5813−5821.

(21) Wines, D.; Choudhary, K.; Tavazza, F. Systematic DFT+U and Quantum Monte Carlo Benchmark of Magnetic Two-Dimensional (2D) CrX_3 (X = I, Br, Cl, F). *J. Phys. Chem. C* **2023**, *127*, 1176−1188.

(22) Tiihonen, J.; Kent, P. R. C.; Krogel, J. T. Surrogate Hessian Accelerated Structural Optimization for Stochastic Electronic Structure Theories. *J. Chem. Phys.* **2022**, *156*, 054104.
(23) Shin, H.; Krogel, J. T.; Gasperich, K.; Kent, P. R. C.; Benali, A.; Heinonen, O. Optimized Structure and Electronic Band Gap of Monolayer GeSe from Quantum Monte Carlo Methods. *Phys. Rev. Materials* **2021**, *5*, 024002.
(24) Staros, D.; Hu, G.; Tiihonen, J.; Nanguneri, R.; Krogel, J.; Bennett, M. C.; Heinonen, O.; Ganesh, P.; Rubenstein, B. A Combined First Principles Study of the Structural, Magnetic, and Phonon Properties of Monolayer CrI_3. *J. Chem. Phys.* **2022**, *156*, 014707.
(25) Hohenberg, P.; Kohn, W. Inhomogeneous Electron Gas. *Phys. Rev.* **1964**, *136*, B864−B871.
(26) Perdew, J. P.; Burke, K.; Ernzerhof, M. Generalized Gradient Approximation Made Simple. *Phys. Rev. Lett.* **1996**, *77*, 3865−3868.
(27) Sun, J.; Ruzsinszky, A.; Perdew, J. P. Strongly Constrained and Appropriately Normed Semilocal Density Functional. *Phys. Rev. Lett.* **2015**, *115*, 036402.
(28) Kresse, G.; Furthmüller, J. Efficient Iterative Schemes for ab initio Total-energy Calculations Using a Plane-wave Basis Set. *Phys. Rev. B* **1996**, *54*, 11169−11186.
(29) Kresse, G.; Joubert, D. From Ultrasoft Pseudopotentials to the Projector Augmented-wave Method. *Phys. Rev. B* **1999**, *59*, 1758−1775.
(30) Grimme, S. Semiempirical GGA-type Density Functional Constructed with a Long-range Dispersion Correction. *J. Comput. Chem.* **2006**, *27*, 1787−1799.
(31) Grimme, S.; Ehrlich, S.; Goerigk, L. Effect of the Damping Function in Dispersion Corrected Density Functional Theory. *J. Comput. Chem.* **2011**, *32*, 1456−1465.
(32) Peng, H.; Yang, Z.-H.; Perdew, J. P.; Sun, J. Versatile van der Waals Density Functional Based on a Meta-Generalized Gradient Approximation. *Phys. Rev. X* **2016**, *6*, 041005.
(33) Dai, J.-Q.; Yuan, J.; Ke, C.; Wei, Z.-C. Tunable Electronic and Magnetic Properties in 1T-VSe_2 Monolayer on $BiFeO_3$(0001) Ferroelectric Substrate. *Appl. Surf. Sci.* **2021**, *547*, 149206.
(34) Kan, M.; Wang, B.; Lee, Y. H.; Sun, Q. A Density Functional Theory Study of the Tunable Structure, Magnetism and Metal-insulator Phase Transition in VS_2 Monolayers Induced by in-plane Biaxial Strain. *Nano Research* **2015**, *8*, 1348−1356.
(35) Kwon, Y.; Ceperley, D. M.; Martin, R. M. Effects of Three-body and Backflow Correlations in the Two-dimensional Electron Gas. *Phys. Rev. B* **1993**, *48*, 12037−12046.
(36) Kwon, Y.; Ceperley, D. M.; Martin, R. M. Effects of Backflow Correlation in the Three-dimensional Electron Gas: Quantum Monte Carlo Study. *Phys. Rev. B* **1998**, *58*, 6800−6806.
(37) López Ríos, P.; Ma, A.; Drummond, N. D.; Towler, M. D.; Needs, R. J. Inhomogeneous Backflow Transformations in Quantum Monte Carlo Calculations. *Phys. Rev. E* **2006**, *74*, 066701.
(38) Bajdich, M.; Tiago, M. L.; Hood, R. Q.; Kent, P. R. C.; Reboredo, F. A. Systematic Reduction of Sign Errors in Many-Body Calculations of Atoms and Molecules. *Phys. Rev. Lett.* **2010**, *104*, 193001.
(39) Ichibha, T.; Dzubak, A. L.; Krogel, J. T.; Cooper, V. R.; Reboredo, F. A. CrI_3 Revisited with a Many-body ab initio Theoretical Approach. *Phys. Rev. Materials* **2021**, *5*, 064006.
(40) Saritas, K.; Krogel, J. T.; Okamoto, S.; Lee, H. N.; Reboredo, F. A. Structural, Electronic, and Magnetic Properties of Bulk and Epitaxial $LaCoO_3$ Through Diffusion Monte Carlo. *Phys. Rev. Materials* **2019**, *3*, 124414.
(41) Saritas, K.; Krogel, J. T.; Kent, P. R. C.; Reboredo, F. A. Diffusion Monte Carlo: A Pathway Towards an Accurate Theoretical Description of Manganese Oxides. *Phys. Rev. Materials* **2018**, *2*, 085801.
(42) Chen, G.; Howard, S. T.; Maghirang, A. B.; Nguyen Cong, K.; Villaos, R. A. B.; Feng, L.-Y.; Cai, K.; Ganguli, S. C.; Swiech, W.; Morosan, E.; Oleynik, I. I.; Chuang, F.-C.; Lin, H.; Madhavan, V. Correlating Structural, Electronic, and Magnetic Properties of Epitaxial VSe_2 Thin Films. *Phys. Rev. B* **2020**, *102*, 115149.
(43) Liu, Z.-L.; Wu, X.; Shao, Y.; Qi, J.; Cao, Y.; Huang, L.; Liu, C.; Wang, J.-O.; Zheng, Q.; Zhu, Z.-L.; Ibrahim, K.; Wang, Y.-L.; Gao, H.-J. Epitaxially Grown Monolayer VSe_2: An Air-stable Magnetic Two-dimensional Material with Low Work Function at Edges. *Science Bulletin* **2018**, *63*, 419−425.
(44) Karn, A.; Chan, Y. H.; Chazarin, U.; Chen, P.; Pai, W. W. Modification of Monolayer 1T-VSe_2 by Selective Deposition of Vanadium and Tellurium. *AIP Advances* **2022**, *12*, 035240.
(45) Song, D.; Zhou, Y.; Zhang, M.; He, X.; Li, X. Structural and Transport Properties of 1T-VSe_2 Single Crystal Under High Pressures. *Front. Mater.* **2021**, *8*, 710849.

https://doi.org/10.1021/acs.jpclett.3c00497
J. Phys. Chem. Lett. 2023, 14, 3553−3560

Supporting Information: A Quantum Monte Carlo Study of the Structural, Energetic, and Magnetic Properties of Two-Dimensional H and T Phase VSe_2

Daniel Wines,[†] Juha Tiihonen,[‡] Kayahan Saritas,[¶] Jaron T. Krogel,[¶] and Can Ataca[*,§]

†*Materials Science and Engineering Division, National Institute of Standards and Technology (NIST), Gaithersburg, MD 20899*

‡*Department of Physics, Nanoscience Center, University of Jyväskylä, P.O. Box 35, Finland*

¶ *Material Science and Technology Division, Oak Ridge National Laboratory, Oak Ridge, Tennessee 37831*

§*Department of Physics, University of Maryland Baltimore County, Baltimore MD 21250*

E-mail: ataca@umbc.edu

Computational Methods

Density functional theory (DFT) benchmarks for the T and H phase of 2D VSe_2 were performed using the Vienna Ab initio Simulation Package (VASP) code with projector augmented wave (PAW) pseudopotentials.[1,2] For these calculations, the local density approximation (LDA),[3] Perdew-Burke-Ernzerhof (PBE),[4] and strongly constrained and appropri-

ately normed (SCAN)[5] meta-GGA functionals were used with the added Hubbard correction (U)[6] to treat the on-site Coulomb interaction of the $3d$ orbitals of the V atoms. At least 20 Å of vacuum was given between periodic layers of VSe_2 in the c-direction. In addition, we used a reciprocal k-point grid of 24x24x1 and a kinetic energy cutoff of 400 eV.

Our Quantum Monte Carlo (QMC) simulations used DFT-PBE to generate the trial wavefunction for fixed-node diffusion Monte Carlo (DMC) calculations. The Quantum Espresso (QE)[7] code was used for our DFT calculations to create the trial wavefunction. This trial wavefunction was created for the ferromagnetic configuration of 2D VSe_2 using different U values with the goal of variationally determining the optimal nodal surface (U value that yields the lowest total energy). For V, we used norm-conserving (NC) RRKJ (OPT) pseudopotentials[8] and for Se, we used NC Burkatzki-Fillipi-Dolg (BFD) pseudopotentials.[9] After testing at the DFT level, a kinetic energy cutoff of 4,080 eV (300 Ry) and a k-point grid of 6x6x1 was used (see Fig. S1 and S2) to generate trial wavefunctions for DMC. To accelerate the line-search method convergence for the metallic T phase, we increased the k-point grid to 12x12x1.

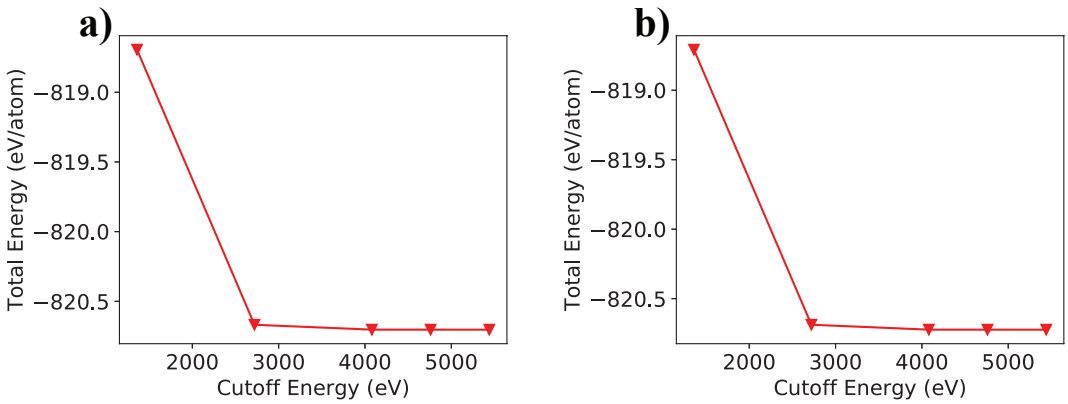

Figure S1: The total energy per atom of the unit cell (3 atoms) of 2D a) T-VSe_2 and b) H-VSe_2 as a function of plane wave cutoff energy for the norm-conserving pseudopotentials calculated with DFT using the PBE functional at a k-point grid of 6x6x1. The results show a converged cutoff energy of 4,080 eV (300 Ry) for both phases.

After the trial wavefunction was generated with DFT, Variational Monte Carlo (VMC) and DMC[10,11] calculations were performed using the QMCPACK[12,13] code. The single de-

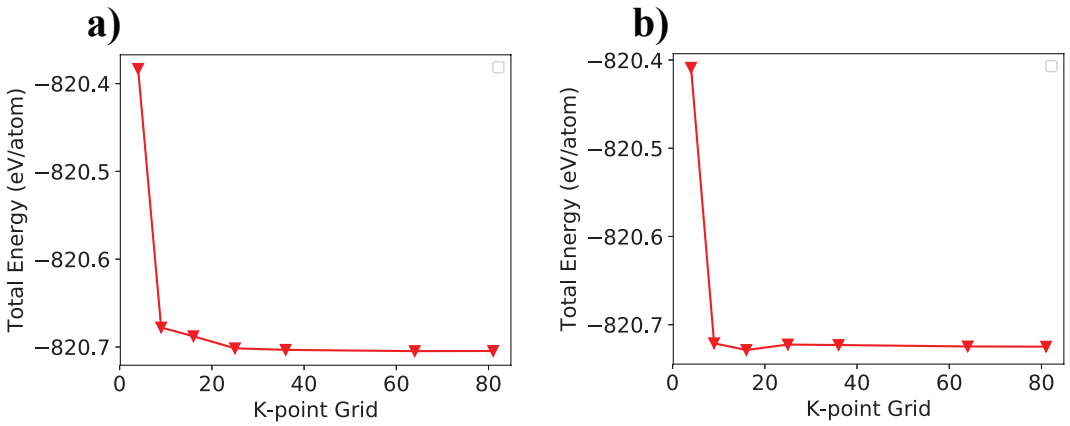

Figure S2: The total energy per atom of the unit cell (3 atoms) of 2D a) T-VSe_2 and b) H-VSe_2 as a function of k-point grid for the norm-conserving pseudopotentials calculated with DFT (PBE) at the converged cutoff energy (see Fig. S1). The results show a converged k-point grid of 6x6x1 (36) for both monolayers. The number of k-points was scaled appropriately to obtain the converged grid depending on the supercell size and shape for all DFT and DMC calculations.

terminant DFT wavefunction is converted into a many-body wavefunction by use of the Jastrow parameters,[14,15] which assist in modeling electron correlation with the goal of reducing the statistical uncertainty in DMC calculations.[16,17] Up to two-body Jastrow[18] correlation functions were included, where the linear method[19] was used to minimize the variance and energy of the VMC energies. The cost function of the variance optimization is 100 % variance minimization and the cost function of the energy optimization is split as 95 % energy minimization and 5 % variance minimization, which has been proven to reduce the uncertainty of DMC calculated results.[16] The Nexus[20] software suite was used to automate the DFT-VMC-DMC workflow. The locality approximation[17] was used to evaluate the nonlocal part of the pseudopotentials in DMC and an optimal timestep of 0.01 Ha^{-1} was determined for DMC simulations due to the fact that it yielded an acceptance ratio greater than 99 % (see Table S1). A full summary of the VMC and DMC methods can be found in reference.[10]

The total charge density and spin density was extracted from our DMC calculations. The spin density is defined as the difference between the spin-up contribution to the total charge density and the spin-down contribution to the total charge density ($\rho_{up} - \rho_{down}$). We

Table S1: Tabulated results for the DMC timestep convergence of a 12 atom cell of 2D T-VSe_2 and H-VSe_2. The acceptance ratio of 0.99 indicates that 0.01 Ha^{-1} is an appropriate timestep to use for all subsequent DMC simulations.

T-VSe_2			
Timestep (Ha^{-1})	DMC Total Energy (Ha)	Error (Ha)	Acceptance Ratio
0.02	-361.730	0.001	0.985
0.01	-361.709	0.002	0.994
0.005	-361.709	0.003	0.997
0.002	-361.702	0.002	0.999
H-VSe_2			
Timestep (Ha^{-1})	DMC Total Energy (Ha)	Error (Ha)	Acceptance Ratio
0.02	-361.673	0.001	0.985
0.01	-361.657	0.002	0.994
0.005	-361.654	0.002	0.998
0.002	-361.657	0.003	0.999

used an extrapolation scheme on the DMC charge densities with the goal of eliminating the bias that occurs from using a mixed estimator. Since the charge density estimator does not commute with the fixed-node Hamiltonian, the DMC charge density was obtained from a mixed estimator between the pure fixed-node DMC and VMC densities. The extrapolation formula takes the form:[10]

$$\rho_1 = 2\rho_{\mathrm{DMC}} - \rho_{\mathrm{VMC}} + \mathcal{O}[(\Phi - \Psi_{\mathrm{T}})^2] \tag{1}$$

where ρ_{DMC} and ρ_{VMC} are the DMC and VMC charge densities respectively. Φ is the trial wavefunction from the DMC Hamiltonian and Ψ_{T} is the trial wavefunction from VMC.

In addition, we integrated the DFT+U and DMC spin densities up to a cutoff radius r_{cut} (which we define as 1.34 Å , due to the fact that it is approximately half of the V-Se bond distance in 2D T and H-VSe_2) in order to estimate the site-averaged atomic magnetic moment per V and Se. To obtain these magnetic moments per atom (M_A), we sum over the spherically interpolated spin densities:

$$M_A = 4\pi \int_0^{r_{cut}} r^2 \rho_s(r) dr \approx 4\pi \sum_{i=0}^{r_{cut}/\Delta r} r_i^2 \rho_s(r_i) \Delta r \tag{2}$$

where r_i is the distance from the center of the atom to a given point on the grid and Δr is the radial grid size.

To optimize the structural parameters of both T and H-VSe_2 according to the DMC potential energy surface (PES), we use a surrogate Hessian accelerated optimization method.[21] In the method, we consider the PES around equilibrium as the second-order expansion in Wyckoff parameter space, p:

$$E(p) = E_0 + \frac{1}{2}(p - p_0)^T H_p (p - p_0), \tag{3}$$

where H_p is the Hessian, or the force-constant matrix, E_0 is the energy minimum and p_0 the energy-minimizing parameters. Diagonalizing the parameter Hessian, i.e., $H_p = U^T \Lambda U$, forms an optimal basis for a conjugate line-search in the parameter space, namely the eigenvectors U. The line-searches along U can be conducted in parallel, and ideally, they locate the minimum in just one parallel iteration within the quadratic region. Here, we conduct the line-search according to a set of 2 parameters: the lattice constant a and the Wyckoff parameter z, which is the unsigned displacement of the Se atoms along the z axis (see Fig. 1). For reporting purposes, the line-search parameters a and z are remapped to a and d, where d is the V-Se distance.

In the surrogate Hessian scheme, we obtain a cheap but relatively accurate Hessian from DFT, and use it to the inform line-search on the DMC PES, in particular by providing the search directions. We also resample the DFT PES to predict fitting errors. Thus, we may minimize the computational cost of the DMC runs, while maintaining an error tolerance. The surrogate DFT PES was based on QE with a 4,080 eV (300 Ry) cutoff using PBE with no DFT+U correction. The DMC PES was based on DFT-PBE with $U = 2$ eV orbitals and finite-size extrapolation through supercell sizes of 9 and 24 atoms. Each line-search was based on a 3rd order polynomial fit and set to contain 7 points, or displaced geometries, totaling 13 energy evaluations per phase, per iteration. However, alternative techniques, including (bi)polynomial fitting, were used in some parts to incorporate auxiliary DMC

data and ensure convergence to the quadratic region. Effectively, two parallel line-search iterations for both phases were carried out, and the convergence was claimed in the absence of significant displacements.

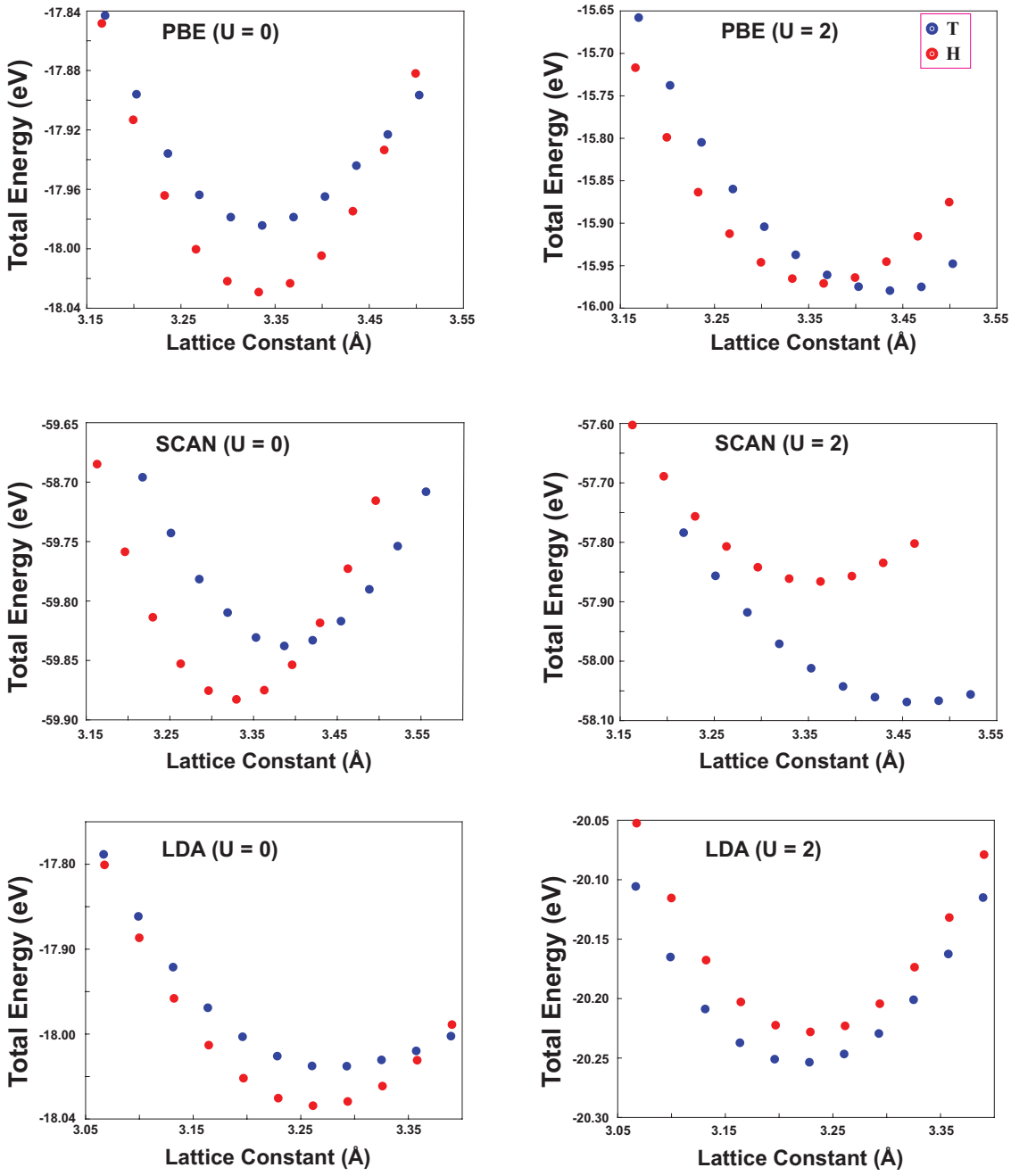

Figure S3: Total energy as a function of lattice strain for T (blue) and H (red) phase 2D VSe_2, calculated with various functionals and U values. Density functionals include LDA, PBE, and SCAN.

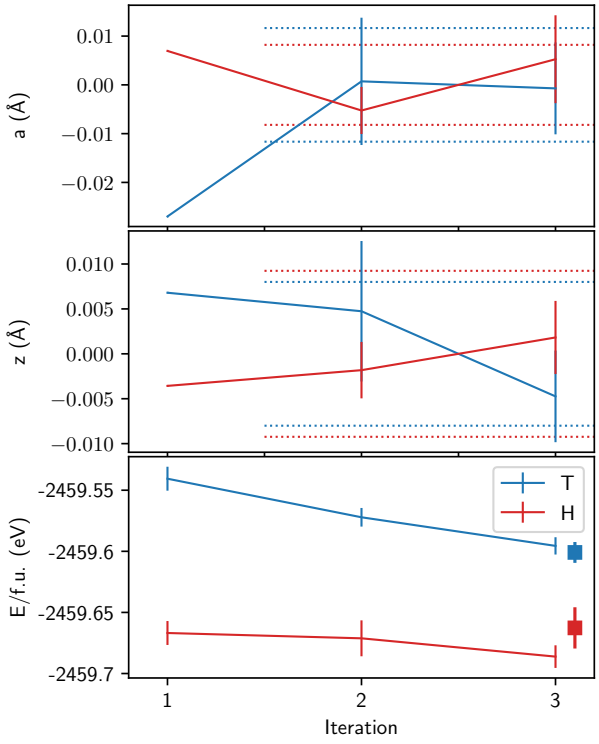

Figure S4: The convergence of the a and z parameters and DMC energies per f.u. for both T (blue) and H (red) phase of 2D VSe_2 based on parallel line-search iterations along the DMC PES. The starting parameters (iteration 1) are from DFT, the zero offset is the mean over iterations 2 and 3, and dotted lines indicate the error tolerances for each case (95 % confidence). The DMC energies from respective equilibrium geometries are plotted with 1SEM (one standard error of the mean) uncertainties, with extra squares marking energies from the predicted minimum geometry.

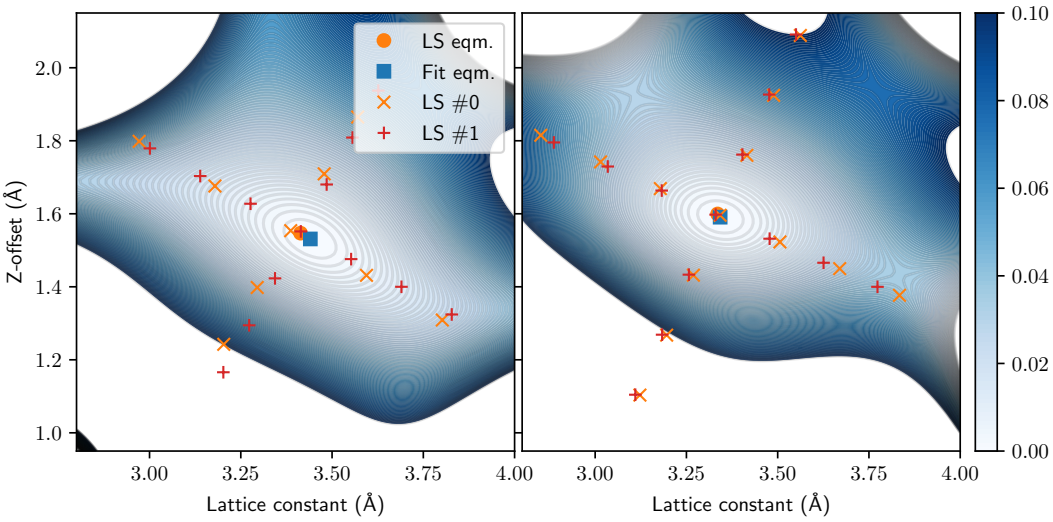

Figure S5: Contour reconstructions of the DMC PESs (eV) of T (left) and H (right) phases of 2D VSe_2 with respect to a and z parameters. The contours are based on bicubic fits to sparse data, and thus, subject to biases and statistical uncertainties not indicated in the figures. The markers ('x' and '+') indicate data points from two parallel line-search (LS) iterations. The circle (LS eqm.) and square (Fit eqm.) represent the line-search minima and the bicubic fit minima, respectively.

References

(1) Kresse, G.; Furthmüller, J. Efficient Iterative Schemes for ab initio Total-energy Calculations Using a Plane-wave Basis Set. *Phys. Rev. B* **1996**, *54*, 11169–11186.

(2) Kresse, G.; Joubert, D. From Ultrasoft Pseudopotentials to the Projector Augmented-wave Method. *Phys. Rev. B* **1999**, *59*, 1758–1775.

(3) Hohenberg, P.; Kohn, W. Inhomogeneous Electron Gas. *Phys. Rev.* **1964**, *136*, B864–B871.

(4) Perdew, J. P.; Burke, K.; Ernzerhof, M. Generalized Gradient Approximation Made Simple. *Phys. Rev. Lett.* **1996**, *77*, 3865–3868.

(5) Sun, J.; Ruzsinszky, A.; Perdew, J. P. Strongly Constrained and Appropriately Normed Semilocal Density Functional. *Phys. Rev. Lett.* **2015**, *115*, 036402.

(6) Dudarev, S. L.; Botton, G. A.; Savrasov, S. Y.; Humphreys, C. J.; Sutton, A. P. Electron-energy-loss Spectra and the Structural Stability of Nickel Oxide: An LSDA+U Study. *Phys. Rev. B* **1998**, *57*, 1505–1509.

(7) Giannozzi, P. et al. QUANTUM ESPRESSO: A Modular and Open-source Software Project for Quantum Simulations of Materials. *J. of Phys.: Cond. Matt.* **2009**, *21*, 395502.

(8) Krogel, J. T.; Santana, J. A.; Reboredo, F. A. Pseudopotentials for Quantum Monte Carlo Studies of Transition Metal Oxides. *Phys. Rev. B* **2016**, *93*, 075143.

(9) Burkatzki, M.; Filippi, C.; Dolg, M. Energy-consistent Pseudopotentials for Quantum Monte Carlo Calculations. *J. Chem. Phys.* **2007**, *126*, 234105.

(10) Foulkes, W. M. C.; Mitas, L.; Needs, R. J.; Rajagopal, G. Quantum Monte Carlo Simulations of Solids. *Rev. Mod. Phys.* **2001**, *73*, 33–83.

(11) Needs, R. J.; Towler, M. D.; Drummond, N. D.; Ríos, P. L. Continuum Variational and Diffusion Quantum Monte Carlo calculations. *J. of Phys.: Cond. Matt.* **2009**, *22*, 023201.

(12) Kim, J. et al. QMCPACK: An Open Source ab initio Quantum Monte Carlo Package for the Electronic Structure of Atoms, Molecules and Solids. *J. of Phys.: Cond. Matter* **2018**, *30*, 195901.

(13) Kent, P. R. C. et al. QMCPACK: Advances in the Development, Efficiency, and Application of Auxiliary Field and Real-space Variational and Diffusion Quantum Monte Carlo. *J. Chem. Phys.* **2020**, *152*, 174105.

(14) Slater, J. C. The Theory of Complex Spectra. *Phys. Rev.* **1929**, *34*, 1293–1322.

(15) Jastrow, R. Many-Body Problem with Strong Forces. *Phys. Rev.* **1955**, *98*, 1479–1484.

(16) Umrigar, C. J.; Filippi, C. Energy and Variance Optimization of Many-Body Wave Functions. *Phys. Rev. Lett.* **2005**, *94*, 150201.

(17) Mitas, L.; Shirley, E. L.; Ceperley, D. M. Nonlocal Pseudopotentials and Diffusion Monte Carlo. *J. Chem. Phys.* **1991**, *95*, 3467–3475.

(18) Drummond, N. D.; Towler, M. D.; Needs, R. J. Jastrow Correlation Factor for Atoms, Molecules, and Solids. *Phys. Rev. B* **2004**, *70*, 235119.

(19) Umrigar, C. J.; Toulouse, J.; Filippi, C.; Sorella, S.; Hennig, R. G. Alleviation of the Fermion-Sign Problem by Optimization of Many-Body Wave Functions. *Phys. Rev. Lett.* **2007**, *98*, 110201.

(20) Krogel, J. T. Nexus: A modular Workflow Management System for Quantum Simulation Codes. *Computer Physics Communications* **2016**, *198*, 154 – 168.

(21) Tiihonen, J.; Kent, P. R. C.; Krogel, J. T. Surrogate Hessian Accelerated Structural Optimization for Stochastic Electronic Structure Theories. *J. Chem. Phys.* **2022**, *156*, 054104.